Characterization by image analysis of materials heterogeneities produced by the Deep Soil Mixing technique

Juba Amrioui, Myriam Duc, Alain Le Kouby, Jeanne-Sylvine Guedon, Lucile Saussaye, Sahar Hemmati, François Willot, Petr Dokládal

Materials Today: Proceedings xxx (xxxx) xxx

Contents lists available at ScienceDirect

Materials Today: Proceedings

journal homepage: www.elsevier.com/locate/matpr

Characterization by image analysis of materials heterogeneities produced by the Deep Soil Mixing technique

Juba Amrioui [a,*], Myriam Duc [a], Alain Le Kouby [a], Jeanne-Sylvine Guedon [a], Lucile Saussaye [b], Sahar Hemmati [a], François Willot [c], Petr Dokladal [c]

[a] Laboratoire GERS/SRO, Université Gustave Eiffel, Marne-la-Vallée, France
[b] Equipe Recherche ENDSUM, Cerema, Blois, France
[c] Centre de Morphologie Mathématique, Centre des Matériaux, Mines Paris – PSL University, Fontainebleau, France

ARTICLE INFO

Article history:
Available online xxxx

Keywords:
Deep Soil Mixing
Characterization of inclusions
Soil-cement matrix
X-ray Computed Tomography
Image analysis
Image segmentation
Artificial intelligence
3D numerical simulation

ABSTRACT

The Deep Soil Mixing (DSM) material is a cementitious composite consisting of a well-mixed soil/cement matrix and may contain unmixed soil inclusions and possibly gravel. To obtain a 3D reconstruction of a DSM specimen structure, a destructive method was investigated, as an alternative to X-Ray Computed Tomography scans. The proposed method is based on image analysis and photographs of few millimeters thickness slices of a specimen. A detailed morphological description of inclusions, including volume fraction, shape, size distribution and spatial arrangement using common image analysis and CAD softwares preceded the validation of the 3D destructive method by the non-destructive X-ray CT based on 3 criteria (volume fraction, size distribution and shadow zone area). Compared to 1D and 2D basic methods found in the literature, the 3D developed method prevented biases linked to the external surface estimation of inclusions' volume fraction. Next, to improve the experimental procedure, an extended methodology was established for estimating the inclusions volume fractions. Such method relies on a database of 3D reconstructed inclusion shapes and on the optimization of the sawing thickness. The aim consisted in the obtaining of unbiased estimates of the volume fractions with fewer cuts, between 4 and 18 instead of 50–60, which made such method as a low-cost, practical and accurate procedure. Finally, the 3D mesh generated by the 3D destructive method was used in numerical approach to propose, as an example, a successful hydromechanical numerical simulation of the DSM material response. Furthermore, a machine learning framework using the 2D slices of specimens produced during the application of the 3D destructive method, was proposed to generate various realistic 3D shapes instead of the usual spherical shape for inclusions, which will allow testing high number of meso-structures in numerical simulation.

Selection and peer-review under responsibility of the scientific committee of the International Conference on Advances in Construction Materials and Structures.

1. Introduction

In order to remedy the risk of failure by internal erosion of the Loire earthen levees, cut-off walls were built using the Deep Soil Mixing (DSM) method [1–5]. The DSM is an in-situ soil improvement process that consists of mixing the soil in place with cement and water. However, the natural soil heterogeneity, combined with the size and rotation speed of the mixing tool, leads to the appearance of unmixed soil inclusions (or balls with various sizes) in the soil–cement mixture. Indeed, previous studies showed that the presence of such unmixed soil inclusions was unavoidable on site [6–10], especially when the soil to be treated was silty or clayey [11–14]. Furthermore, the quantity, size, shape, and the random distribution of soil clumps can simultaneously affect mechanical and/or hydraulic properties of hardened DSM material and explains why results obtained on laboratory-made materials differ from those coming from the site [15–20]. The quantification of unmixed soil inclusions (or even their complete characterization) is therefore necessary to anticipate potential long-term problems and contribute to the improvement of the DSM implementation technique to ensure a better mixing quality.

Numerous research works in the literature take the time to explain the use features of the DSM process in the improvement of the bearing capacity of clayey soils [21–24], supporting struc-

* Corresponding author.
E-mail addresses: amriouijuba@yahoo.fr, juba.amrioui@univ-eiffel.fr (J. Amrioui).

https://doi.org/10.1016/j.matpr.2023.03.720
2214-7853/
Selection and peer-review under responsibility of the scientific committee of the International Conference on Advances in Construction Materials and Structures.

tural foundations [25–28] or waterproofing [29–33]. However, the effect of soil inclusions not mixed with cement is rarely mentioned [15,16,17,19,20,34,35]. Laefer et al. [15] reported that unmixed clay with cement even in small amounts (about 1%) can significantly reduce the compressive strength and stiffness of DSM made by the jet grouting technique. Moreover, the higher the amount of inclusions in the DSM material, the greater the reduction in performance [16,17,20,34]. Furthermore, Vervoort et al. [34] and Van Lysebetten et al. [19] performed a pure parametric study using 2D numerical modeling to investigate the effect of inclusion characteristics (variables quantity, shape, size, and relative position) on the mechanical strength as well as the stiffness of DSM samples. The results showed that angular inclusions have a more detrimental impact on strength and stiffness than did rounded inclusions. In addition, a large inclusion of unmixed soil with cement in a DSM specimen can reduce the strength and stiffness by more than three times compared to a specimen containing smaller inclusions with similar shape and volume fraction. Finally, it was reported in these studies that soil inclusions oriented at 26° to the cylinder axis and distributed in a clustered form have a more negative effect on the mechanical response than inclusions oriented along the cylinder axis and distributed in a more homogeneous manner.

In latter studies, the volume fraction of inclusions was assessed using two non-destructive methodologies, denoted "1D" and "2D method", developed in Belgium based on tests on cores collected in situ or on whole sections of columns/screens performed by the DSM process [11,16,36]. The "1D method" is a simple procedure that can be used manually on site. It consists of measuring the cumulative length of the inclusions on four generating lines drawn on the lateral surface of cylindrical DSM specimens. The "2D method", described in detail by Denies et al. [16], is performed using image analysis to evaluate the surface fraction of inclusions. This method has been enhanced by Amrioui et al. [35] by applying semi-automatic image segmentation tools and extended to treat the lateral surface of cylindrical specimens, allowing one to extract additional information, such as the 2D inclusions surface fractions, their (2D) size distribution, relative position in the DSM matrix as well as the location of the digitized inclusion contours. However, given the complex distribution of soil inclusions within the DSM matrix, the representativeness of such statistics, derived from observations of the external surface of cylindrical specimens, has not been assessed. More sophisticated 3D imaging techniques are required to address the accuracy of the non-destructive methods.

Recently, X-ray CT has gained considerable momentum in the field of civil engineering. Indeed, it has been widely used to generate 3D numerical models of concrete with realistic internal structure to simulate permeability test [37–39], chloride ion diffusing ability [40], elastic [41] and elastoplastic behaviour with damage evolution to failure of material [42–45]. As described by latter authors, the X-ray CT ternary images were first segmented into three phases according to appropriate grey value thresholds. Then, after morphological and manual transforms such as filtering noise from the images [37,40], removing contacts between gravels and voids in the matrix [42,44], and holes closing [44], a 3D model has been generated from a stack of segmented 2D slices. This workflow is often performed using the *ImageJ* software [37,38,39,40,46,47]. As reported in the literature, the image transforms are time and CPU-consuming. Huang et al. [42] proposed to use an image compression algorithm that provides a good balance between the accuracy of the reconstructed morphology and computational cost.

Other methods to characterize heterogeneous materials include the work of Nagai et al. [48] who proposed a procedure for obtaining a 3D mesh of a concrete based on a set of 2D images segmented by thresholding the grayscale images and removing fine gravels. Sequential images were obtained by cutting a specimen using a diamond scraper and a computer flatbed scanner. Based upon the same principle, Yue et al. [49] treated 256 images photographed by a camera after sawing a specimen of asphalt concrete. After automatic adjustment of the threshold value, the large gravels, incorporated in the bituminous matrix, were segmented and vectorized to model the indirect tensile test, also known as Brazilian test. In the field of cementitious materials, analysing real images photographed with a camera or a digital scanner is a delicate and tedious step, especially when the binder phase is greyish. Nagai et al. [48] reported an improvement of the image processing steps after using red Fe_2O_3 to highlight the cementitious matrix, while Song et al. [46] enhanced the image contrast using phenolphthalein, which turns pink in contact with the cementitious paste with basic character.

Currently, studying the impact of unmixed soil inclusions on hydromechanical properties of DSM material is based on the quantification of such clumps using the "1D" and "2D method" developed in the literature, assuming that both methods are unbiased. In the present work, which is part of the strengthening of Loire dykes by the DSM process and whose material produced contains soil inclusions in more or less important percentages depending on the type of soil to be treated [35], a new methodology is proposed to characterize 3D inclusions in an effort to validate (or infirm) the results provided by methods found in literature (1D and 2D method). An X-ray CT test was performed on a DSM specimen from the site to obtain a 3D image of the soil inclusions and gravels. As X-ray CT gave an unpromising result for characterizing DSM materials, a new method, denoted "3D method", was developed for the 3D reconstruction of unmixed soil inclusions and gravels based on the analysis of images acquired by the specimen's destruction. The method implemented using standard image processing and CAD softwares was validated by comparing the reconstructed 3D image of gravels with that from X-ray CT. The innovating aspect of the proposed "3D method" was the ability to investigate the DSM material heterogeneity within the specimen volume with a more realistic approach, whereas the "1D" and "2D method" inspected the outer lateral surface of cylindrical specimens [11,16,35,36], which may be fundamentally biased. At the same time, it allowed the reconstruction of the 3D image of the analyzed specimens with fewer cuts compared to previous studies [48,49]. Furthermore, based on the stereological principle, a more practical, faster, and representative method to evaluate the inclusions volume fractions was established based on the optimizing of the sawing thickness and the making use of a database of 3D reconstructions. The objective was to estimate the inclusions volume fraction in an unbiased way with the least number of cuts, i.e., between 4 and 18 cuts instead of 50 or 60. Moreover, in a step to exploit the "3D method" results in the numerical approaches, a 3D shape prediction work of inclusions by Artificial Intelligence using the complex 2D shapes set identified on the slices after image processing was presented as a new way of estimation. Finally, the inclusion meso-structure, reconstructed using the "3D method" and exported as a 3D mesh, was used to run a numerical simulation example to calculate the hydromechanical response of the DSM material using COMSOL Multiphysics software.

2. Materials and experimental procedure

2.1. Preparation of the DSM samples

Vertical core drillings of 100 mm diameter, down to a depth of 6 to 8 m, were carried out along the whole height of DSM cut-off walls made on the Loire dikes. Cylindrical specimens of 100 mm diameter and 200 mm height (slenderness 2) were cut to characterize the sampled materials. The cores were cut with a circular

saw under water. The specimens were stored at 20 °C with a relative humidity of 85% in a double hermetic envelope to avoid drying. Despite these precautions, a browning of the initially bluish cementitious matrix appeared on the specimen's surface in contact with air during storage.

2.2. Three-dimensional characterization of DSM samples by X-ray computed tomography

To visualize the different phases composing the DSM material (matrix, soil inclusions and gravels), an X-ray CT feasibility test was performed on a 10 cm diameter and 20 cm high specimen. To perform scans, a Ultratom microtomograph made by Rx Solutions was used, including a L10801Hamamatsu source and an PaxScan4343DX-I imager. Scan parameters were 200 kV, 300 μA for the source and 1 fps and an averaging of 12 images for the imager.

Fig. 1a shows an example of an X-ray CT scan of a DSM specimen. From the CT scan, gravels (light grey zones) can be differentiated from the embedding matrix. Besides gravels, darker (black) zones represented the unconnected macroporosity or cracks in the binder phase of the material, which was an information of great interest as very large pores between 1 and 15 mm could not be identified by local mercury intrusion porosimetry (MIP) measurements exploring 3 nm to 100 μm pores on samples volume less than 1 cm^3. Although the unmixed soil inclusions (phase 2 in Fig. 1b) appeared more porous compared to matrix as well as the matrix-inclusion interface, most soil inclusions could not be distinguished from the CT scans. X-ray CT technique principle explained such results. Indeed, the calculation of the X-ray absorption coefficient which is a function of the density and chemical composition of the analysed material [40,50] could not separate phases. For illustration, Table 1 summarizes the true density values of the matrix, soil inclusions and different types of gravels differentiated visually on specimens from the site. As comparison between the X-ray CT scans and pictures of 2D cuts show that neither the limestone gravels, nor the soil inclusions, clearly appeared by contrast in matrix (Fig. 2) because of similar density around 2400 kg/m^3.

The 3D image of gravels other than limestone as well as that of macropores were reconstructed from the 2D X-ray CT scans on *Fiji-ImageJ* software. The 2597 acquired slices were initially converted to gray scale (8-bit). Then, three light intensity profiles on three locations in the 2D slice in Fig. 1a were plotted to determine the optimal threshold in gray value to segment the different phases, i.e., gravels (Fig. 3a), macropores (Fig. 3b), and soil inclusions (Fig. 3c) from the DSM material matrix. Fig. 3a and b show that for gravels and macropores, a sufficient contrast allowed defining two distinct thresholds. However, Fig. 3c shows a relatively constant gray level between matrix and soil inclusions. It means that unmixed soil with cement could not be segmented from the matrix in any way, even if the soil-matrix interface was well marked.

Finally, despite the very good resolution of images, X-ray tomography did not visualize unmixed soil inclusions and limestone gravels in the tested site specimens. However, X-ray tomography remains efficient in the case of DSM specimens that contain soil inclusions made in the laboratory by adding a "tracer or marker" (heavier chemical element) to the inclusions to create a high-enough density contrast to highlight them by tomography.

2.3. Development of a three-dimensional characterization method for soft soil inclusions

- **Cutting and image acquisition**

Since X-ray tomography is not able to visualize the 3D soil inclusions required to model the DSM materials performance, a new "3D method" was developed. This method consists of cutting the DSM specimen with a circular saw into slices of about 3 mm thickness (Fig. 4a), after performing mechanical and hydraulic tests for performance estimation. The fresh slices were photographed using a Nikon D5600 camera under uniform lighting (Fig. 4b).

- **Segmentation**

Compared to X-ray CT scans, which are often binary or ternary in grey value, the digital camera images are usually composed of a large variety of pixels with a wide range of colors depending on the present mineral phases. Visual observations identified different types of gravels with various colors, such as yellow limestone, white or orange quartz and brown or ochre sandstone. The finding of the optimal threshold value to isolate soil inclusions was attempted (Fig. 5) but the different segmentation techniques used in the literature did not seem to be promising on images of DSM material fresh cuts. For example, the conversion of photos (Fig. 5a) to gray level (Fig. 5b) caused confusion between soil inclusions and orange quartz gravels or brown sandstone, preventing the gray level segmentation application. Although a ternary image was possible by adjusting the tonal range of the real image, the soil inclusions as well as the orange and brown colored gravels were

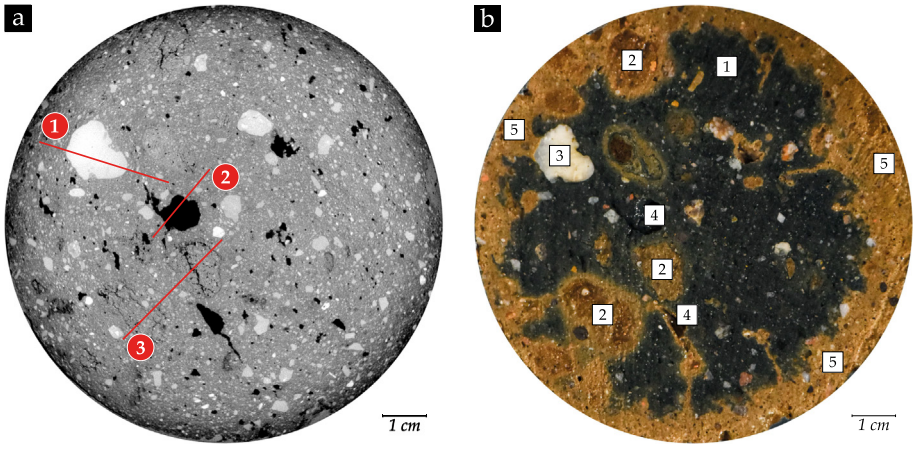

Fig. 1. (a) 2D X-ray CT scan of the DSM specimen with the three lines for the gray level profiles: (1) matrix-gravel-matrix, (2) matrix-void-matrix, (3) matrix-soil-matrix; (b) Photograph of a fresh section of the tested specimen at the same location as in the 2D CT scan showing different phases: (1) matrix, (2) soil inclusions, (3) gravels, (4) macropores, (5) grayish matrix.

Table 1
Values of the true density of the various phases composing the tested DSM specimens derived from mercury intrusion porosimetry (MIP).

Phases	Matrix	Soil inclusions	Limestone	Quartz	Sandstone
Real density (kg/m^3)	2432	2440	2450	2650	2700

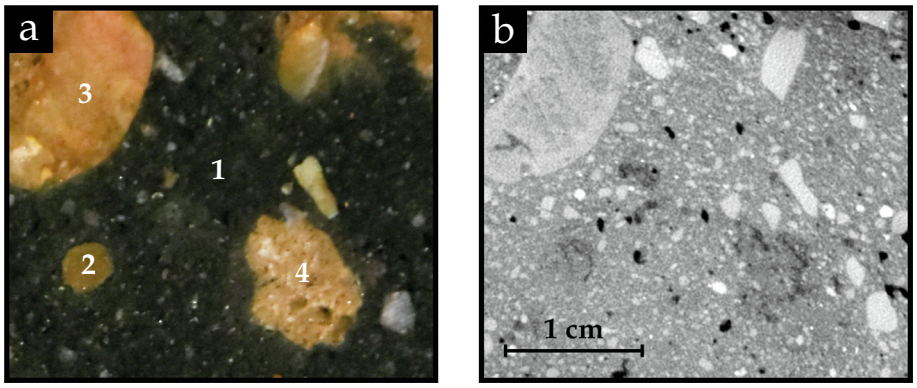

Fig. 2. (a) Photograph of the various phases composing the DSMmaterial: (1) matrix, (2) soil inclusion, (3) orange quartz gravel, (4) yellow limestone gravel; ((b) corresponding X-ray tomography scan. (For interpretation of the references to color in this figure legend, the reader is referred to the web version of this article.)

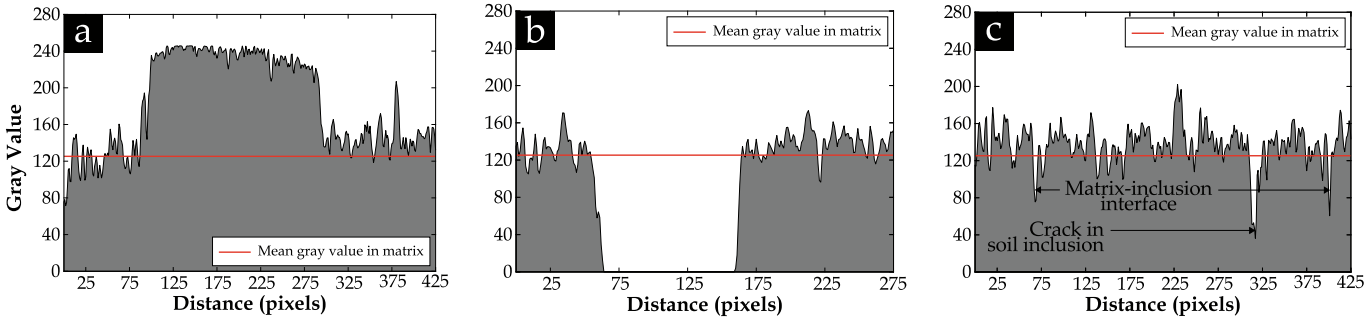

Fig. 3. Three gray level profiles drawn along three lines: (a) matrix-gravel-matrix; (b) matrix-void-matrix; (c) matrix-soil-matrix.

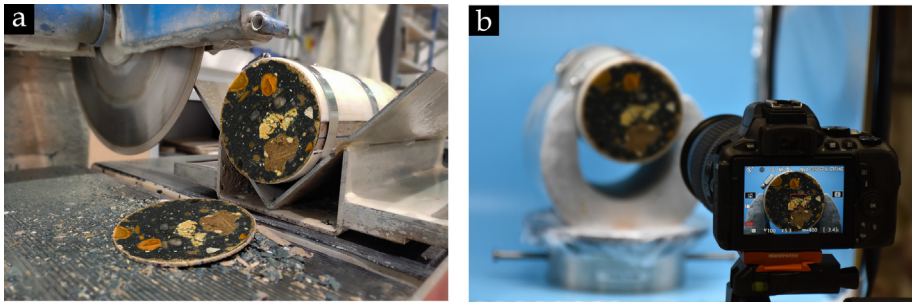

Fig. 4. (a) Cutting of specimens into 3 mm slices using an underwater material saw; (b) Image acquisition using a digital camera.

switched to red color as observed on Fig. 5c. Even in this case, the confusion remained between phases.

Since automated image processing has not been successful, a new segmentation procedure based on photo editing software was proposed, in which human appreciation supplied the phases differencing. The first step of digitizing the inclusions operated on *Adobe Photoshop* software. It involved selecting the soil inclusions as well as the gravels (size $\geq$ 2 mm) using the *Magic Wand* tool. The two selected types of inclusions were then isolated from the matrix on two separate layers. To differentiate between soil and gravels in the matrix, three colors were assigned to each phase: dark blue to the matrix, brown to the soil inclusions, and yellow to all gravels (Fig. 6b). Finally, both layers were separately exported in *.jpeg* or *.png* format and produced images were vectorized to digitize the geometry contours using *Adobe Illustrator* software (Fig. 6b) while calibrating the scale at 1:1. The exported vectorized images in *.dxf* format were compatible and executable on CAD software (*Autocad* and *SolidWorks*).

- **3D reconstruction**

The 3D reconstruction procedures described in the literature are highly dependent on the spacing between the 2D images, i.e., a stepped shape can appear remarkably if the spacing is very large.

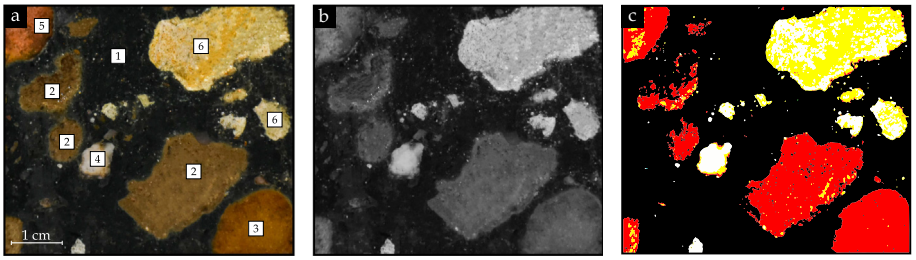

Fig. 5. (a) Rectangular section of a photographed image of the DSMfresh cut containing: (1) matrix, (2) soil inclusions, (3) orange quartz, (4) white quartz, (5) brown sandstone, (6) yellow limestone; (b) same image converted to grayscale; (c) after adjustment of the image tonal range. (For interpretation of the references to color in this figure legend, the reader is referred to the web version of this article.)

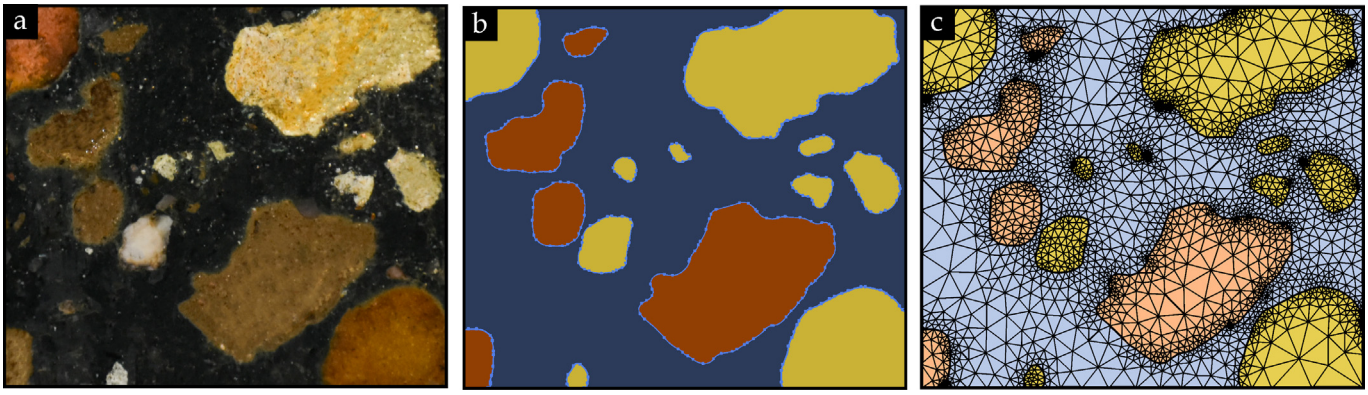

Fig. 6. (a) Rectangular section of a photographed image of the fresh cut; (b) Vectorized ternary image using *Adobe Illustrator* software to generate *.dxf* files; (c) Example of a mesh using *COMSOL Multiphysics* software.

The new 3D reconstruction procedure for DSM specimens proposed in this paper is based on the *Boundary Boss or base* smoothing function used in *SolidWorks* software. This function creates 3D geometry from a set of 2D sketches with larger spacing than usually found in X-ray CT or even in the traditional destructive methods of specimens imaging [48,49]. Profiles containing the 2D contours of inclusions (soil or gravels) were first imported into *SolidWorks* (Fig. 7a). Then, using the smoothing function, the 3D space bounded by the 2D contours was filled to reproduce the volume of the inclusion (Fig. 7b–c). At the end, a 3D image of the soil inclusions and gravels was generated in *.stl* or *.ply* format (Fig. 7d). The volume and size distribution of inclusions can be determined from the 3D mesh using the *Autodesk Netfabb* software.

The 3D percentage of inclusions can be estimated by calculating the sum of the elementary volumes obtained from the area of inclusions multiplied by the thickness of the slices without having to reconstruct their 3D image. It is the same principle of stacking by transforming 2D pixels into 3D voxels. However, here the voxel size is about 3 mm. The volume percentage is the total volume of inclusions over the total volume of the specimen using Eq. (1).

$$P_{3D} = 100 \times \frac{V}{V_t} = 100 \times \frac{\sum_{i=1}^{N} A_i.e_i}{V_t} \quad (1)$$

where V is the total calculated volume of inclusions, A_i is the area of inclusions on profile i, e_i is the thickness of slice i measured after a sawing operation using a grouting foot and V_t is the volume of the specimen.

- **Validation of the "3D method"**

The DSM specimen scanned by X-ray CT was characterized by the "3D method" developed in this study. Both 3D images of gravels obtained were compared according to three criteria in order to validate the "3D method", namely the volume fraction, the shadow zone area and the size distribution. Fig. 8a-b shows two 3D images of gravels obtained by the non-destructive and destructive methods with volume fractions of 6% and 6.2% respectively. The slight difference found between both values is due to the limestone gravels not reconstructed in the case of X-ray CT. The volume fraction of gravels calculated by Eq. (1) is about 6.4%. It turns out that this estimate is larger than the total volume of inclusions given the

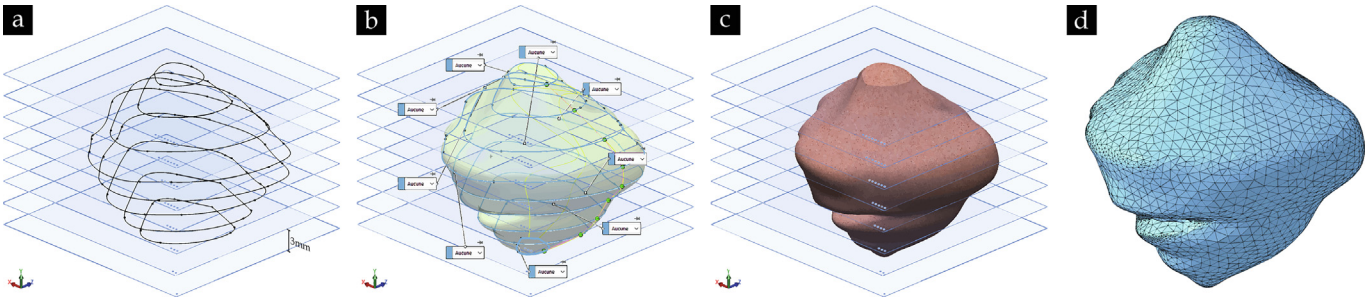

Fig. 7. (a) 2D inclusion profiles inserted in their corresponding planes on *SolidWorks*; (b) *Boundary Boss or base* function; (c) 3D reconstructed inclusion; (d) Example of 3D mesh of an inclusion on *Autodesk Netfabb*.

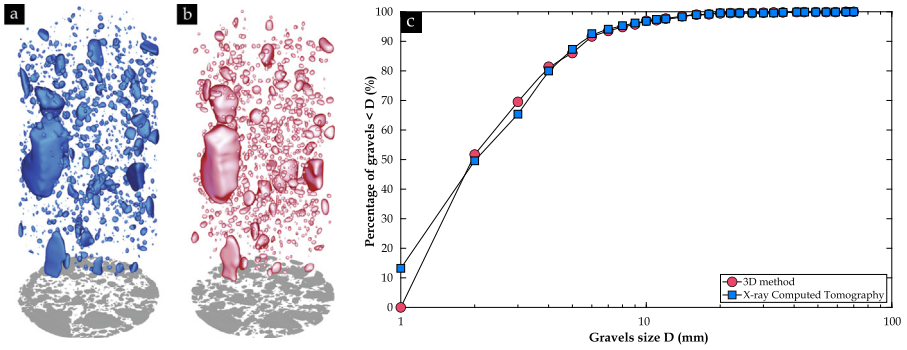

Fig. 8. (a) 3D image of gravels obtained by X-ray CT; (b) 3D image of the same gravels obtained by the "3D method"; (c) Cumulative gravel size distribution in the two 3D images obtained by X-ray CT and "3D method".

stepped shape considered in the calculation of elemental volumes. The shadow zone area of the 3D images was also compared. It is based on the orthogonal projection of the gravels on the bottom plane of the 3D geometries (Fig. 8a and b). This area, which provides the layout of the 3D forms created within specimen space, represents 63.7% and 66.3% of the cross section of the specimen reconstructed by X-ray CT and "3D method" respectively.

The size-distribution of gravels, for both 3D reconstructed images, were determined on *Autodesk Netfabb* software and shown in Fig. 8c. A superposition of the two curves can be observed when the gravel size is higher or equal to 2 mm. As expected, gravels with size of 1 mm are not considered by the "3D method" due to the image resolution. However, the amount of gravels with size of 3 mm is slightly higher in the geometry obtained by the "3D method". This can be attributed to the fact that, at a position on the specimen axis, some gravels with size of 2 mm on the (x,z) plane can have a size of 3 mm after reconstruction along the y axis, this size corresponds to the thickness of the slice.

3. Experimental results and discussions

3.1. Evaluation of inclusions volume fractions in DSM materials

The volume fractions of inclusions (unmixed soil and gravels) evaluated based on the "1D method" developed by Denies et al. [16], the "2D method" improved by Amrioui et al. [35], and the "3D method" developed in this paper, are plotted in Fig. 9. Regardless of evaluation method and specimen origin, the amount of unmixed soil inclusions and gravels varies between 0 and 48%. First, the comparison of the two 1D and 2D non-destructive methods shows that the linear fractions are higher than the surface ones (Fig. 9a). Then, the comparison of these fractions and volume fractions evaluated using the "3D method" shows, as expected, that scattered results with no direct link between the "3D method", considered here as the reference, and the 1D (Fig. 9b) or 2D (Fig. 9c) methods. Moreover, the manual "1D method", known for its simplicity, overestimates the percentages more remarkably than the "2D method". Thus, finally, it turns out that the "1D" and "2D method" currently used in construction sites by DSM are biased, and the development of a new simpler, more practical, and more realistic method is strongly recommended.

To interpret the variance of the results shown in Fig. 9, a Poisson-Boolean set of inclusions (see [51]) is considered as a model for the dispersion of gravel in the material. To simplify the analysis, monodisperse spherical inclusions were generated. The variance D_d^2 of the apparent volume fraction is computed on a set Ω_d reads (see [52]):

$$D_d^2(P) = \frac{(1-P)^2}{|\Omega_d|}\int_{t\in\Omega_d} d^d t\left[(1-P)^{-k(t)}-1\right] \tag{2}$$

where $|\Omega_d|$ is the measure of Ω_d (length, surface or volume in dimensions $d=[1,2,3]$), and:

$$k(t) = \begin{cases} 1-(3/2)(t/a)+(1/2)(t/a)^3 & t \le a \\ 0 & t \ge a \end{cases} \tag{3}$$

is the normalized covariogram of spheres, equal to the proportion of the volume of a sphere of diameter a intersected by the same sphere translated at a distance t. Taking for Ω_d a line of length $2R$ ($d=1$), a disk and a ball of radius R ($d=2$ and 3) one obtains:

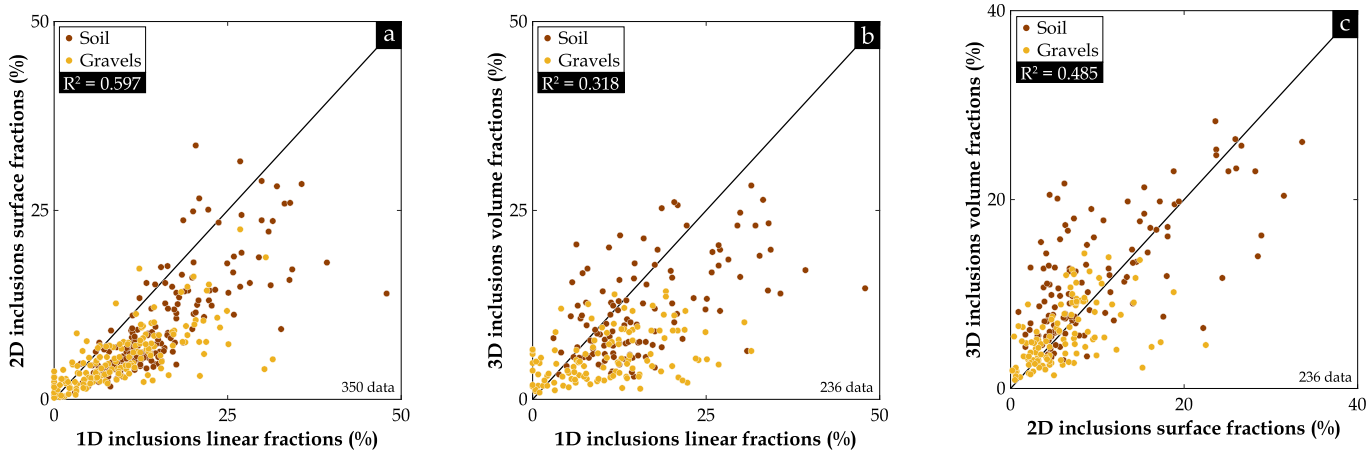

Fig. 9. (a) Surface versus linear fractions of inclusions evaluated on the lateral surface of the DSM specimens; (b and c) Volume fractions versus linear and surface fractions of inclusions respectively.

$$D_d^2(P) = \mu_d(1-P)^2(a/R)^d \int_{s=0}^{1} ds^{d-1}\left[(1-P)^{s(3-s^2)/2-1} - 1\right] \quad (4)$$

with $\mu_1 = \mu_2 = 1$, $\mu_3 = 3$. The integral above admits no simple solution but may be computed numerically or approximated by expanding the integrand to order 2 in s when $s \to 0$. We let $a = 15mm$, $P = 25\%$ and choose R so that the measure of Ω_d coincides with experiments: $R = 4 \times H(d=1)$, $\pi R^2 = 2\pi LH(d=2)$ and $4/3\pi R^3 = \pi L^2 H$ where $L = 50$ mm and $H = 200$ mm are the radius and height of the cylinder and define the absolute error as $\varepsilon_d = 2\sqrt{D_d^2}$ [53]. We obtain $\varepsilon_1 = 7\%$, $\varepsilon_2 = 3\%$ and $\varepsilon_3 = 2\%$ in dimensions 1, 2 and 3. These values are comparable to numerical estimates obtained from 1,000 random configurations of the Boolean set generated in a cylindrical domain (see Fig. 10a). The distribution of the corresponding errors for the 4 lines along the lateral surface of the cylindrical specimen ($d = 1$), the lateral surface of the cylindrical specimen ($d = 2$) and the cylinder ($d = 3$) yield respectively, $\varepsilon_1 = 9\%$, $\varepsilon_2 = 4\%$ and $\varepsilon_3 = 2.6\%$. These errors are smaller than those obtained in the real specimens but confirm a much narrower distribution for the "3D method" compared to the "2D" and "1D method" and a significant difference between the three methods.

3.2. Towards a "simplified 3D method"

The database provided by the "3D method" was used to feed a statistical approach as a step towards the development of a new "simplified 3D method". It is recalled that the volume fractions were determined from cuttings with an average thickness of 3 mm. New volume fractions were calculated from the same database considering spacings greater than 3 mm: 10, 15, 20, 25, 30, 35, 40, 45 mm. The aim was to apply the stereological principle of Delesse, according to Weibel [54], to allow an unbiased evaluation of the volume fraction with fewer cuttings, i.e., to average the 2D percentages over 4 to 18 photographed images instead of 50 or even 65 images per 20 cm high specimen using equation (5).

$$P_{3D}(e) = 100 \times \frac{\sum_{i=1}^{N} P_{2D}^i}{N(e,H)} \quad (5)$$

where P_{2D}^i is the 2D surface fraction of inclusions on the cuts spaced by e along the y axis of the specimens (P_{2D}^i are derived from the curves shown in Fig. 10b and c), $N(e,H)$ is the number of cuts considered as a function of thickness e and the specimen height H.

The resulting 3D volume fractions were then compared to the real ones, as shown in Fig. 11. The points in grey represent the 3D volume fractions calculated using the 2D surface fraction curves as a function of the position y of the cutting along the specimen axis as described by Weibel [54]. The curves $P_{2D} = f_n(y)$ in Fig. 10c were plotted from polynomials f_n of degree n greater than or equal to 20 in order to reproduce the same random aspect seen in the 2D surface fractions profiles of soil inclusions and gravels ($P_{2D} = g(y)$ in Fig. 10b). Such results show that, even with thicker cuttings ($10 \leq e \leq 45$ mm), the volume percentages of inclusions remain relatively unchanged especially for thicknesses ≤ 30 mm. It means that we can considerably reduce the time needed to evaluate the 3D volume fractions of inclusions.

3.3. Prediction of 3D solids from 2D sections by artificial intelligence

Previous work on vector representation has demonstrated the 3D generative and predictive capability of a latent space obtained using the T-Net architecture [55]. It has been shown its ability to predict a voxel-representation of 3D shape of everyday life objects (chair, table, ...) from a photograph providing a partial 2D information of this object.

While the 3D shapes of the inclusions (unmixed soil and gravel) can be hypothesized to also be predictable from the 2D sections given in Fig. 6b. However, everyday objects like furniture have a conventional form (e.g., a chair has always four legs, a seat and a backrest) that can be learnt by the model to aid the inference from a photograph. Contrarily to that, a 2D section of inclusions contains only partial information about their 3D morphology which is completely arbitrary. In order to aid the inference of 3D shapes, the T-Net architecture [55] was adapted to input three sections (instead of one) to infer a single form (see Fig. 12).

Although X-ray CT and the new "3D method" developed in this study allow the construction of complex shapes, the available database of 3D inclusions is very limited. To counter the absence of complex 3D shapes of inclusions, a database of simple and synthetic shapes was created using a ShapeGenerator [56] and then voxelized via Voxelizer [57]. In this way, a library of 250 synthetic shapes with different morphological properties is obtained. From this library of basic shapes, a method to generate complex shapes was proposed. To diversify the morphological properties, spatial transformations such as rotation, translation, size change and inversion were applied. The shapes obtained after these transformations undergo unions by two, thus, a new shape was con-

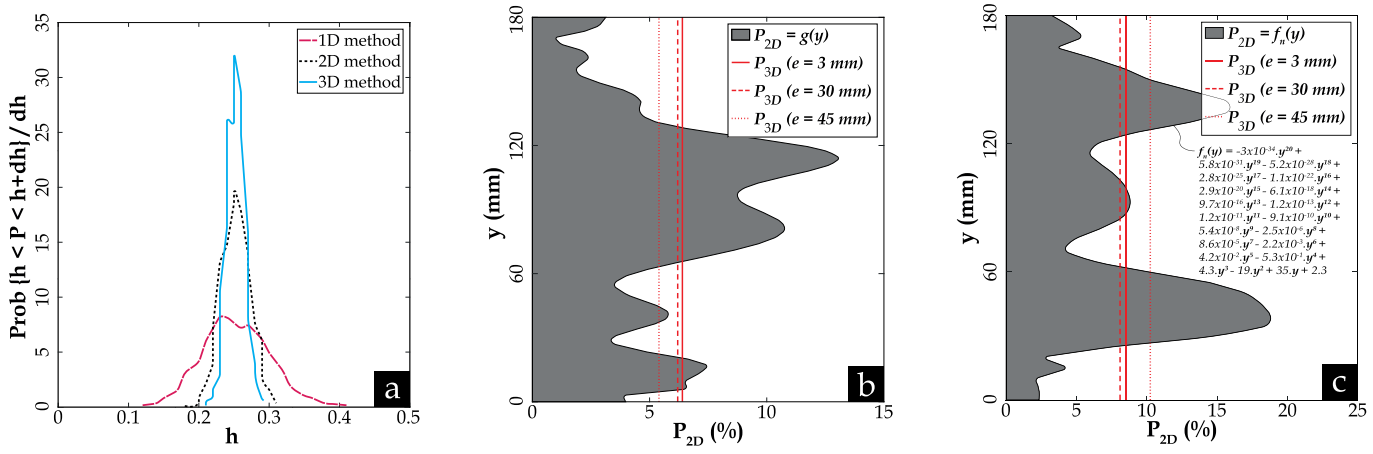

Fig. 10. (a) Probability distribution of the volume fraction P of inclusions in a Boolean model, estimated using the "1D", "2D" and "3D method"; (b–c) Variation of the 2D surface fraction of inclusions as a function of y-position along the specimen axis and comparison between the volume fractions estimated at 3, 30 and 45 mm spacings: case of a real DSM specimen and case of an artificial specimen represented by a polynomial of degree 20 respectively.

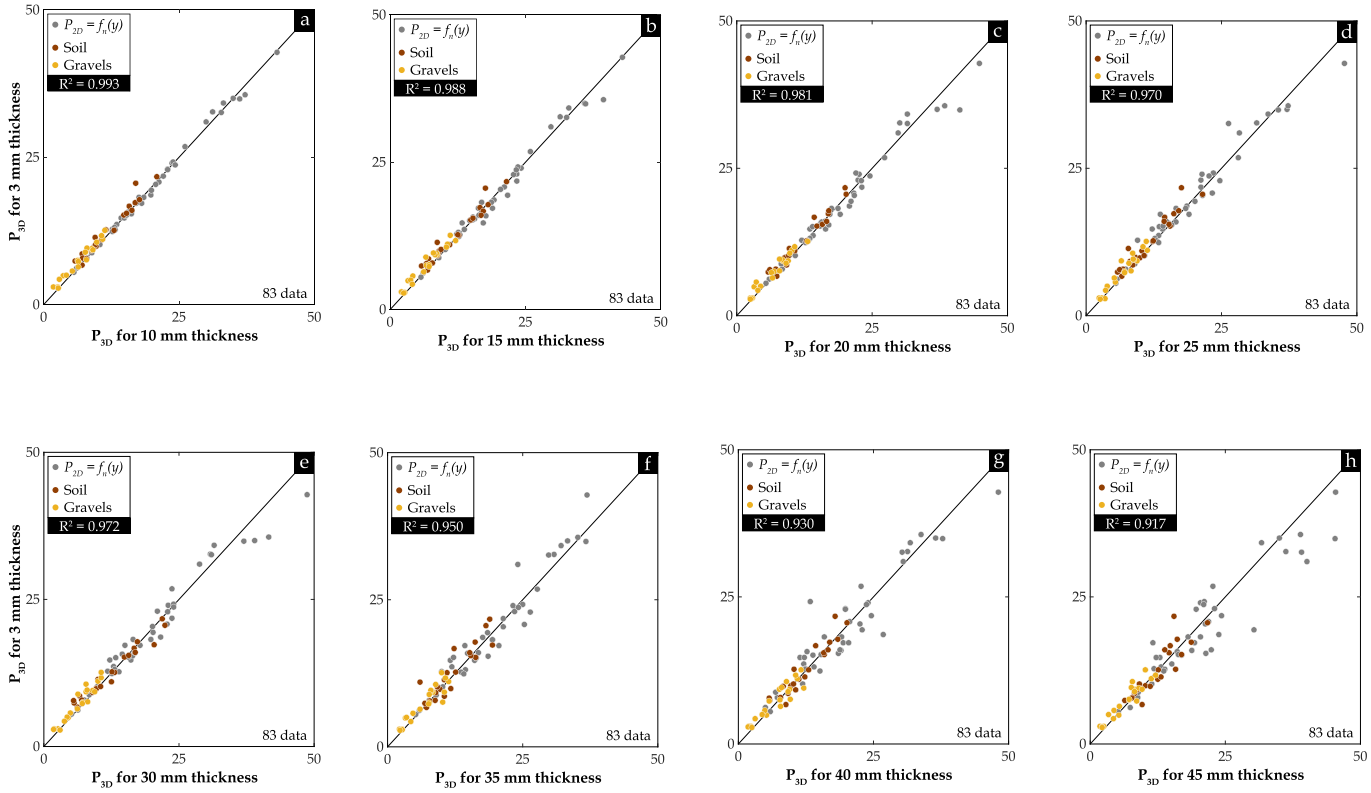

Fig. 11. Real 3D volume fractions calculated considering all 3 mm cuttings versus 3D volume fractions calculated on cuttings at spacings of (a) 10 mm; (b) 15 mm; (c) 20 mm; (d) 25 mm; (e) 30 mm; (f) 35 mm; (g) 40 mm; (h) 45 mm.

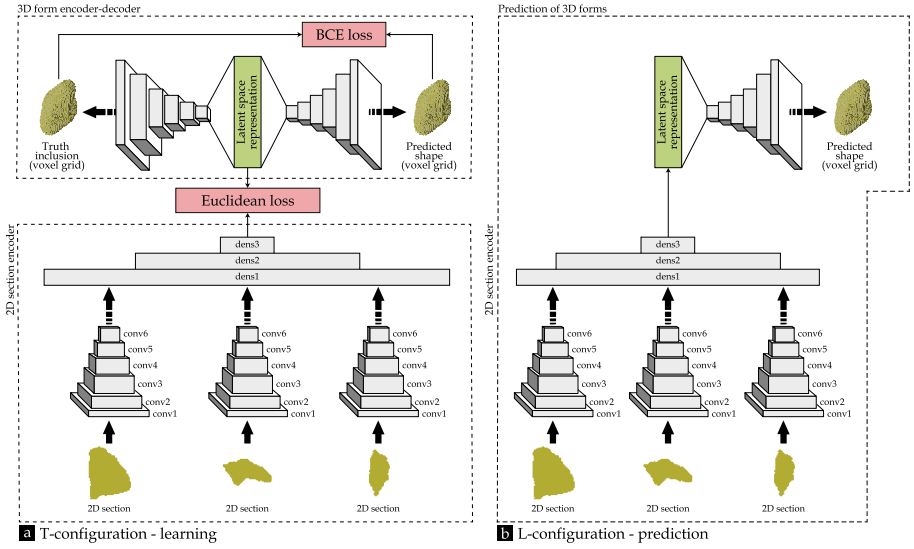

Fig. 12. T-Net architecture (inspired from [55]).

structed from two transformed shapes. Furthermore, non-convex shapes can be generated.

- **Results: Simulation of DSM core models**

After training the T-Net model in the setup given by Fig. 12a, a latent space capable of generating complex and non-convex 3D shapes from triplets of sections was obtained. The image processing on sections (Fig. 6) allowed the consolidation of a database containing a set of 2D shapes of inclusions that exist in the DSM material. Subsets of three 2D sections of real inclusions were selected and presented to the model in the configuration on Fig. 12b. Soil inclusions and gravels were generated separately respecting the granulometry that defines the real size of inclusions and the choice of sections (which cut represents which axis of space). The selection is randomized to ensure that the generated

shape is plausible, i.e. that it respects the properties in 2D and 3D space of real inclusions.

The generated inclusions were used to generate a DSM core model in a cylinder of diameter 100 mm and height 160 mm. Following the particle size distribution of the inclusions, from coarse to fine, the generated inclusions were randomly inserted. With a probability of 0.5, a soil inclusion or gravel was inserted. The insertion of inclusions is without contact, i.e. every new inclusion is placed in a free space. Considering a theoretical volume fraction of soil inclusions and gravel, when the volume fraction is reached for either phase, the phase insertion will be stopped. An example of artificial DSM core is presented in Fig. 13. Each phase is presented separately to simplify reading.

3.4. Example of 3D numerical simulation of the hydromechanical response of the DSM material

To better understand the effect of soil inclusions on the hydromechanical properties of DSM materials, numerical simulation may be one of the most promising solutions. Although there is some research on the effect of soil inclusions on mechanical response of soil–cement mixtures. However, the numerical calculations in these studies were often performed in 2D [11,17,19,34] and possibly in 3D considering spherical inclusions [20]. The "3D method" developed in this paper allows to generate 3D real geometries of inclusions that can be used for numerical modelling. Fig. 14 shows a simulation example of a water permeability and an unconfined compressive strength (UCS) test for a DSM specimen containing soil inclusions not mixed with cement, without considering the interfacial transition zone (ITZ). Indeed, in the presence of only 8% soil ball, the water permeability of the DSM specimen was increased by four times and its compressive strength was reduced by two. Indeed, this drop in performance can be more significant if ITZ was considered [58–62].

4. Conclusions and perspectives

This study falls within the framework of strengthening the Loire dykes by the DSM process, and whose material produced during the progress can contain inclusions of soil not mixed with cement in variable percentages according to the nature of the soil to be treated. Results from the literature showed that the quantity, size, shape and random distribution of soil inclusions affect simultaneously the mechanical and/or hydraulic performance of hardened DSM materials. Characterizing these inclusions is therefore necessary to anticipate possible long-term problems and to help improve the technique of DSM material processing. The main objective of this work was thus to implement a new methodology to characterize the inclusions in 3D and to propose a comparison with the results obtained from the previous methods (1D and 2D method). As a first step, based on several DSM specimens from construction sites in France, this study showed that X-ray Computed

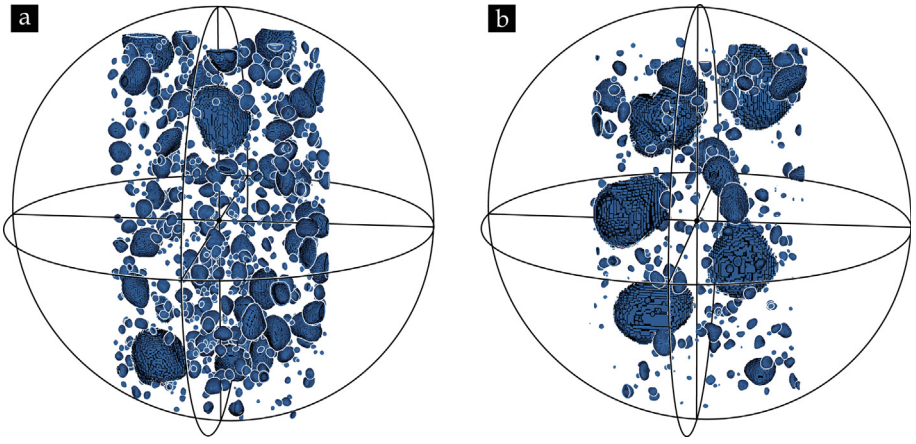

Fig. 13. Generation of a DSM model: (a) soil inclusions; (b) gravels with volume fraction of 8.3% and 7.3% respectively.

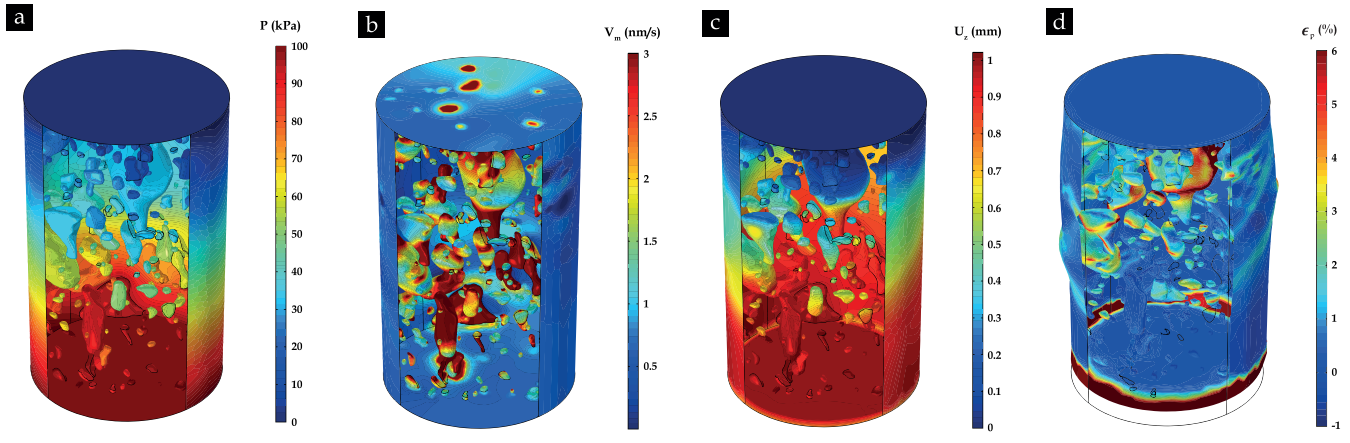

Fig. 14. Simulation of the water permeability test: (a) water pressure applied at the bottom and top of the DSM sample; (b) average flow velocity; Simulation of the unconfined compressive strength test: (c) displacement applied along the z-axis; (d) effective plastic strain after failure.

Tomography, although it offers high image resolution, cannot identify soil inclusions in the DSM matrix, as the density and chemical composition of these two phases are very close. A new procedure to characterize these soil balls, inevitably present on site, was therefore presented. The "3D method" was based on the destruction of specimens, image processing and 3D reconstruction using photo editing and CAD software. Indeed, although it does not consider inclusions smaller than 2 mm and provides more rounded shapes, this method was validated based on the 3D image of the gravels from the X-ray CT scan. The comparison between the "1D" and "2D method", developed in the literature, and the "3D method", considered as a reference, showed that both non-destructive methods (1D and 2D) applied on lateral surface of cylindrical specimens are relatively biased, but can remain interesting for qualitative analyses. Furthermore, a statistical approach was adopted to implement a faster method than the 3D one to assess the inclusions volume fractions. It consists in the median of the evaluated 2D percentages on the specimen cuttings, considering an optimal spacing of less than or equal to 30 mm instead of 3 mm, which involves many cuttings to be processed. In addition, the volume fraction database from the "3D method" will be used in another approach to set up new methodologies for quantifying inclusions on DSM specimens in situ. Indeed, this approach must offer a procedure that requires less material, less work time, and above all can be easily applied on site.

Although the mechanical behavior of DSM materials was studied numerically in the literature. However, the authors in most studies used 2D models or even 3D models but containing spherical inclusions. The 3D reconstruction procedure presented in this paper provides real 3D meso-structures that can be used to run numerical simulations, as shown in the previous example. Moreover, to finely study the effect of the inclusion (soil or gravel) characteristics (quantity, shape, size spatial arrangement that are difficult to be controlled experimentally) on the hydromechanical response of DSM materials, the 2D shapes from image processing was used to predict 3D meso-structures by artificial intelligence. Indeed, generating sufficient 3D models of inclusions will allow to evaluate the magnitude of the expected variations of DSM material performance and to assess the most unfavorable cases. These numerical models, once validated by experimental results, can be directly transposed to DSM structures in situ (cut-off walls/columns).

CRediT Author Contribution statement

J. Amrioui: Conceptualization, Methodology, Software, Visualization, Writing – original draft, Writing – review & editing. **M. Duc:** Conceptualization, Supervision, Writing – review & editing. **A. Le Kouby:** Conceptualization, Supervision, Writing – review & editing. **J.-S. Guedon:** Supervision. **L. Saussaye:** Supervision. **S. Hemmati:** Supervision, Software. **F. Willot:** Supervision, Software, Writing – original draft. **P. Dokladal:** Supervision, Software, Writing – original draft.

Data availability

Data will be made available on request.

Declaration of Competing Interest

The authors declare that they have no known competing financial interests or personal relationships that could have appeared to influence the work reported in this paper.

Acknowledgements

The XRCT device of laboratoire Navier used in this study has benefitted from the financial support of Region Ile de France (SESAME program and DIM/MAP project).

References

[1] A. Le Kouby, M. Duc, J. Marino-Paredes, S. Fanelli, Multi-scale approach of clay soil treatment by the Deep Soil Mixing method, in: Proceedings of 8th national days of geotechnics and engineering geology, Nancy, France, 2016, 8 p.
[2] A. Le Kouby, M. Duc, F. Szymkiewicz, S. Shen, Impact of soil type, cement content, water content on mechanical and porosity properties on cement treated materials, in: Proceedings of 9th national days of geotechnics and engineering geology, Champs-sur-Marne, France, 2018, 8 p.
[3] A. Le Kouby, L. Saussaye, M. Duc, Impact of physical properties of soil on mechanical properties of soil cement treated materials, in: Proceedings of 10th national days of geotechnics and engineering geology, Lyon, France, 2020, 8 p.
[4] L. Saussaye, A. Le Kouby, F. Mathieu, J.F. Mosser, Reinforcement of levees by Deep Soil Mixing technique – case history of tours Loire area, Proceedings of 9th national days of geotechnics and engineering geology, Champs-sur-Marne, France, 2018, 8 p.
[5] S. Patouillard, L. Saussaye, E. Durand, N. Manceau, A. Le Kouby, A. Coulet, Deep Soil Mixing feedback in Loire levees, in: Proceedings of maritime and river dikes for flood protection 3rd Colloquium, France Aix-en-Provence, 2019, 8 p.
[6] A. Porbaha, State of the art in quality assessment of deep mixing technology, Proc. Instit. Civil Engineers – Ground Improvem. 6 (3) (2002) 95–120, https://doi.org/10.1680/grim.2002.6.3.95.
[7] S. Horpibulsk, R. Rachan, A. Suddeepong, A. Chinkulkijniwat, Strength development in cement admixed Bangkok Clay: laboratory and field investigations, Soils Found. 51 (2) (2011) 239–251, https://doi.org/10.3208/sandf.51.239.
[8] S. Horpibulsuk, R. Rachan, A. Suddeepong, State of the art in strength development of soil–cement columns, Proc. Instit. Civil Engineers – Ground Improvem. 165 (4) (2012) 201–215, https://doi.org/10.1680/grim.11.00006.
[9] S. Pooranampillai, D. Parmantier, K. Dawson, S. Shin, A case history on the design, construction, and field quality control of cement Deep Soil Mixing, in: Proceedings of 37th Annual conference on deep foundations, 2012, pp. 135–145.
[10] P. Jamsawang, P. Voottipruex, P. Boathong, W. Mairaing, S. Horpibulsuk, Three-dimensional numerical investigation on lateral movement and factor of safety of slopes stabilized with deep cement mixing column rows, Eng. Geol. 188 (2015) 159–167, https://doi.org/10.1016/j.enggeo.2015.01.017.
[11] P. Ganne, N. Denies, N. Huybrechts, A. Vervoort, A. Tavallali, J. Maertens, B. Lameire, F. De Cock, Soil mix: influence of soil inclusions on structural behaviour, in: Proceedings of the 15th European Conference on Soil Mechanics and Geotechnical Engineering, 2011, pp. 977–982. 10.3233/978-1-60750-801-4-977.
[12] A. Guimond-Barrett, Influence of mixing and curing conditions on the characteristics and durability of soils stabilized by deep mixing, PhD thesis, Université du Havre, (2013), 262 p, tel-02497429.
[13] M. Nozu, M. Sakakibara, N.T. Ahn, Securing of in-situ cement mixing quality for the expansive soil with the "montmorillonite" inclusion, in: Proceedings of conference deep mixing, San Francisco, USA, 2015, pp. 845–852.
[14] L. De Vos, M. De Beukelaer-Dossche, L. Vincke, E. Dupont, K. Duyck, N. Huybrechts, N. Denies, Application of soil mixing (CSM) in stiff clay for dike stabilization, in: Proceedings of the XVII ECSMGE-2019, Geotechnical Engineering foundation of the future, 2019. 10.32075/17ECSMGE-2019-0316.
[15] D.F. Laefer, D. O'Neill, C. O'Mahony, Impact of clay on early jet grouting strength, in: Proceedings of DFI 34th Annual Conference on Deep Foundations, Kansas City USA, 2009.
[16] N. Denies, N. Huybrechts, A. Vervoort, J. Maertens, Mechanical characterization of deep soil mix material, procedure description, in: Proceedings of TC211 International Symposium on Ground Improvement IS-GI, 2012, pp. 117–126.
[17] P. Ganne, N. Denies, N. Huybrechts, A. Vervoort, A. Tavallali, J. Maertens, B. Lameire, F. De Cock, Deep Soil Mix technology in Belgium: Effect of inclusions on design properties, in: Proceedings of the Fourth International Conference on Grouting and Deep Mixing, 2012, pp. 357–366. 10.1061/9780784412350.0021.
[18] N. Denies, G. Van Lysebetten, N. Huybrechts, F. De Cock, B. Lameire, J. Maertens, A. Vervoort, Design of Deep Soil Mix Structures: considerations on the UCS characteristic value, in: Proceedings of the 18th International Conference on Soil Mechanics and Geotechnical Engineering, Paris, France, Vol. 3, 2013, pp. 2465–2468.
[19] G. Van Lysebetten, A. Vervoort, J. Maertens, N. Huybrechts, Discrete element modelling for the study of the effect of soft inclusions on the behaviour of soil mix material, Comput. Geotech. 55 (2014) 342–351, https://doi.org/10.1016/j.compgeo.2013.09.023.
[20] J.J. Hessouh, J. Eslami, A.-L. Beaucour, O. Helson, A. Noumowe, P. Gotteland, Study of effect of soft inclusion on the mechanical behaviour of soilcrete mixtures: experimental and modelling approaches, Mater. Struct. 51 (5) (2018), https://doi.org/10.1617/s11527-018-1264-2.
[21] D.T. Bergado, T. Ruenkrairergsa, Y. Taesiri, A.S. Balasubramaniam, Deep soil mixing used to reduce embankment settlement, Proc. Institut. Civil Engineers-

Ground Improvem. 3 (4) (1999) 145–162, https://doi.org/10.1680/gi.1999.030402.
[22] S.-L. Shen, N. Miura, H. Koga, Interaction mechanism between deep mixing column and surrounding clay during installation, Can. Geotech. J. 40 (2) (2003) 293–307, https://doi.org/10.1139/t02-109.
[23] Y. Hong, X. Wu, P. Zhang, Construction Technology and Mechanical Properties of a Cement-Soil Mixing Pile Reinforced by Basalt Fibre, Adv. Mater. Sci. Eng. (2017) 1–14, https://doi.org/10.1155/2017/9736465.
[24] G. Ye, H. Shu, Z. Zhang, S. Kang, S. Zhang, Q. Wang, Solidification and field assessment of soft soil stabilized by a waste-based binder using deep mixing method, Bull. Eng. Geol. Environ. 80 (6) (2021) 5061–5074, https://doi.org/10.1007/s10064-021-02193-7.
[25] A. Porbaha, H. Tanaka, M. Kobayashi, State of the art in deep mixing technology: part II. Applications, Proc. Institut. Civil Engineers-Ground Improvem. 2 (3) (1998) 125–139, https://doi.org/10.1680/gi.1998.020303.
[26] M. Topolnicki, General overview and advances in Deep Soil Mixing, in: Proceedings of the XXIV Geotechnical Conference of Torino Design, Construction and Controls of Soil Improvement Systems, Torino, Italy, 2016, 30 p.
[27] C. Jung, R. Ceglarek, T. Clauvelin, M. Ayeldeen, D. Kim, Deep Soil Mixing in Sabkha Soils for Foundation Support in United Arab Emirates, Int. J. Geosynth. Ground Eng. 6 (1) (2020), https://doi.org/10.1007/s40891-020-0188-4.
[28] Y. Liu, Q. Zhang, R. Liu, P. Jiang, Z. Wang, X. Wang, D. Gui, Numerical Simulation and Field Monitoring of Deformation Characteristics of TRD Composite Supporting Structure for Deep Foundation Pit in Quaternary Stratum: A Case Study in Qingdao, Geotech. Geol. Eng. 40 (5) (2022) 2691–2703, https://doi.org/10.1007/s10706-022-02054-4.
[29] P. Falaciński, K. Garbulewski, Z. Kledyński, Z. Skutnik, K. Ziarkowska, Fluidised fly-ash cement-bentonite cut-off walls in flood protection, Archiv. Hydro-Eng. Environ. Mech. 52 (1) (2005) 7–20.
[30] R. Kuś, D. Słowikowski, Zastosowanie wybranych technologii uszczelniania podłoża gruntowego w budownictwie hydrotechnicznym–wieloletnie doświadczenia PRGW, in: Proceedings of the European Symposium Anti-Flood Defences, Paris-Orléans, France, 2012, 8 p. (In Polish).
[31] D. Alós Shepherd, E. Kotan, F. Dehn, State of the Art Report - Plastic Concrete for Cut-Off Walls. Institute of Concrete Structures and Building Materials (IMB). Materials Testing and Research Institute (MPA Karlsruhe). Karlsruhe Institute of Technology. Karlsruhe, (2018), 68p. 10.5445/IR/1000085901.
[32] Z. Skutnik, M. Bajda, M. Lech, The selection of sealing technologies of the subsoil and hydrotechnical structures and quality assurance, Open Eng. 9 (1) (2019) 420–427, https://doi.org/10.1515/eng-2019-0050.
[33] Cfbr, Recueil de méthodes et de techniques de confortement et réparation des digues de protection en remblai, Comité Français des Barrages et Réservoirs (2021) 501.
[34] A. Vervoort, A. Tavallali, G. Van Lysebetten, J. Maertens, N. Huybrechts, Mechanical characterization of large-scale soil mix samples and the analysis of the influence of soil inclusions, in: Proceedings of TC211 International Symposium on Ground Improvement IS-GI, 2012, pp. 127–135.
[35] J. Amrioui, A. Le Kouby, M. Duc, J.-S. Guedon, L. Saussaye, Impact of soil inclusions in the Deep Soil Mixing material matrix, in: Proceedings of 11th national days of geotechnics and engineering geology, France, Lyon, 2022, 8 p.
[36] BBRI, Handbook Soil mix walls, Taylor and Francis Group, (2018), ISBN 978 90 5367 6441 7.
[37] X. Sun, Q. Dai, K. Ng, Computational investigation of pore permeability and connectivity from transmission X-ray microscope images of a cement paste specimen, Constr. Build. Mater. 68 (2014) 240–251, https://doi.org/10.1016/j.conbuildmat.2014.06.049.
[38] M. Zhang, Pore-scale modelling of relative permeability of cementitious materials using X-ray computed microtomography images, Cem. Concr. Res. 95 (2017) 18–29, https://doi.org/10.1016/j.cemconres.2017.02.005.
[39] J. Zhang, G. Ma, R. Ming, X. Cui, L. Li, H. Xu, Numerical study on seepage flow in pervious concrete based on 3D CT imaging, Constr. Build. Mater. 161 (2018) 468–478, https://doi.org/10.1016/j.conbuildmat.2017.11.149.
[40] Y. Tian, C. Chen, N. Jin, X. Jin, Z. Tian, D. Yan, W. Yu, An investigation on the three-dimensional transport of chloride ions in concrete based on X-ray computed tomography technology, Constr. Build. Mater. 221 (2019) 443–455, https://doi.org/10.1016/j.conbuildmat.2019.05.144.
[41] J. Escoda, F. Willot, D. Jeulin, J. Sanahuja, C. Toulemonde, Estimation of local stresses and elastic properties of a mortar sample by FFT computation of fields on a 3D image, Cem. Concr. Res. 41 (5) (2011) 542–556, https://doi.org/10.1016/j.cemconres.2011.02.003.
[42] Y. Huang, Z. Yang, W. Ren, G. Liu, C. Zhang, 3D meso-scale fracture modelling and validation of concrete based on in-situ X-ray Computed Tomography images using damage plasticity model, Int. J. Solids Struct. 67–68 (2015) 340–352, https://doi.org/10.1016/j.ijsolstr.2015.05.002.
[43] Y. Huang, D. Yan, Z. Yang, G. Liu, 2D and 3D homogenization and fracture analysis of concrete based on in-situ X-ray Computed Tomography images and Monte Carlo simulations, Eng. Fract. Mech. 163 (2016) 37–54, https://doi.org/10.1016/j.engfracmech.2016.06.018.
[44] Z. Yang, W. Ren, R. Sharma, S. McDonald, M. Mostafavi, Y. Vertyagina, T.J. Marrow, In-situ X-ray computed tomography characterisation of 3D fracture evolution and image-based numerical homogenisation of concrete, Cem. Concr. Compos. 75 (2017) 74–83, https://doi.org/10.1016/j.cemconcomp.2016.10.001.
[45] M. Nitka, J. Tejchman, A three-dimensional meso-scale approach to concrete fracture based on combined DEM with X-ray μCT images, Cem. Concr. Res. 107 (2018) 11–29, https://doi.org/10.1016/j.cemconres.2018.02.006.
[46] Y. Song, R.M. Damiani, C. Shen, D.I. Castaneda, D.A. Lange, A 3D petrographic analysis for concrete freeze-thaw protection, Cem. Concr. Res. 128 (2020), https://doi.org/10.1016/j.cemconres.2019.105952.
[47] Y. Sargam, K. Wang, Quantifying dispersion of nanosilica in hardened cement matrix using a novel SEM-EDS and image analysis-based methodology, Cem. Concr. Res. 147 (2021), https://doi.org/10.1016/j.cemconres.2021.106524.
[48] G. Nagai, T. Yamada, A. Wada, Stress analysis of concrete material based on geometrically accurate finite element modeling, in: Proceedings of Third International Conference on Fracture Mechanics of Concrete and Concrete Structures (FRAMCOS-3), Vol. 42, 1998, pp. 1077–1086.
[49] Z.Q. Yue, S. Chen, L.G. Tham, Finite element modeling of geomaterials using digital image processing, Comput. Geotech. 30 (5) (2003) 375–397, https://doi.org/10.1016/s0266-352x (03)00015-6.
[50] H.-K. Man, J.G.M. Mier, Size effect on strength and fracture energy for numerical concrete with realistic aggregate shapes, Int. J. Fract. 154 (1–2) (2008) 61–72, https://doi.org/10.1007/s10704-008-9270-y.
[51] G. Matheron, J. Serra, Image analysis and mathematical morphology, Academic Press, London, 1982.
[52] F. Willot, Mean covariogram of cylinders and applications to Boolean random sets, J. Contemp. Math. Anal. (Am. Acad. Sci.) 52 (6) (2017) 305–315, https://doi.org/10.3103/S1068362317060061.
[53] T. Kanit, S. Forest, I. Galliet, V. Mounoury, D. Jeulin, Determination of the size of the representative volume element for random composites: statistical and numerical approach, Int. J. Solids Struct. 40 (13–14) (2003) 3647–3679, https://doi.org/10.1016/s0020-7683(03)00143-4.
[54] E.R. Weibel, Stereological methods in cell biology: where are we-where are we going?, J Histochem. Cytochem. 29 (9) (1981) 1043–1052, https://doi.org/10.1177/29.9.7026667.
[55] R. Girdhar, D.F. Fouhey, M. Rodriguez, A. Gupta, Learning a predictable and generative vector representation for objects, in: Proceedings of European Conference on Computer Vision, 2016, pp. 484–499. 10.48550/arXiv.1603.08637.
[56] Performative Design: Web App Preview - poly3d. Available online at https://drajmarsh.bitbucket.io/poly3d.html (accessed on January 5, 2023).
[57] Drububu.com: Online Voxelizer. Available online at https://www.drububu.com/miscellaneous/voxelizer/index.html?out=obj (accessed on January 5, 2023).
[58] J.P. Ollivier, J.C. Maso, B. Bourdette, Interfacial transition zone in concrete, Adv. Cem. Bas. Mat. 2 (1) (1995) 30–38, https://doi.org/10.1016/1065-7355(95)90037-3.
[59] H.S. Wong, M. Zobel, N.R. Buenfeld, R.W. Zimmerman, Influence of the interfacial transition zone and microcracking on the diffusivity, permeability and sorptivity of cement-based materials after drying, Mag. Concr. Res. 61 (8) (2009) 571–589, https://doi.org/10.1680/macr.2008.61.8.571.
[60] X. Li, Q. Xu, S. Chen, An experimental and numerical study on water permeability of concrete, Constr. Build. Mater. 105 (2016) 503–510, https://doi.org/10.1016/j.conbuildmat.2015.12.184.
[61] X. Li, Y. Xu, S. Chen, Computational homogenization of effective permeability in three-phase mesoscale concrete, Constr. Build. Mater. 121 (2016) 100–111, https://doi.org/10.1016/j.conbuildmat.2016.05.141.
[62] M. Liang, K. Feng, C. He, Y. Li, L. An, W. Guo, A meso-scale model toward concrete water permeability regarding aggregate permeability, Constr. Build. Mater. 261 (2020), https://doi.org/10.1016/j.conbuildmat.2020.120547.